HOKKAIDO UNIVERSITY

Title	Influence of macro-fractures and micro-fractures on permeability and elastic wave velocities in basalt at elevated pressure
Author(s)	Nara, Yoshitaka; Meredith, Philip George; Yoneda, Tetsuro et al.
Citation	Tectonophysics, 503(1-2), 52-59 https://doi.org/10.1016/j.tecto.2010.09.027
Issue Date	2011-04-25
Doc URL	https://hdl.handle.net/2115/46107
Type	journal article
File Information	Tec503-1-2_52-59.pdf

Influence of macro-fractures and micro-fractures on permeability and elastic wave velocities in basalt at elevated pressure

Yoshitaka NARA

Rock and Ice Physics Laboratory, Department of Earth Sciences, University College London, Gower Street, London WC1E 6BT, UK.

e-mail: y.nara@ucl.ac.uk

Graduate School of Engineering, Hokkaido University, Kita 13 Nishi 8, Kita-ku, Sapporo 060-8628, Japan.

e-mail: nara@geo-er.eng.hokudai.ac.jp

Philip George MEREDITH

Rock and Ice Physics Laboratory, Department of Earth Sciences, University College London, Gower Street, London WC1E 6BT, UK.

e-mail: p.meredith@ucl.ac.uk

Tetsuro YONEDA

Graduate School of Engineering, Hokkaido University, Kita 13 Nishi 8, Kita-ku, Sapporo 060-8628, Japan.

e-mail: yonet@eng.hokudai.ac.jp

Katsuhiko KANEKO

Graduate School of Engineering, Hokkaido University, Kita 13 Nishi 8, Kita-ku, Sapporo 060-8628, Japan.

e-mail: kaneko@geo-er.eng.hokudai.ac.jp

Corresponding author: Yoshitaka NARA

Postal address: Rock and Ice Physics Laboratory, Department of Earth Sciences, University College

London, Gower Street, London WC1E 6BT, UK.

e-mail: y.nara@ucl.ac.uk, TEL: +44-20-7679-0404, FAX: +44-20-7679-2433

Abstract

Fractures are ubiquitous on all scales in crustal rocks. The investigation of fractures and their influence on physical and transport properties of rocks is therefore essential for understanding of many key problems in seismology, volcanology and rock engineering. In crystalline rocks, pore water is primarily stored in and migrates through networks of cracks and fractures at all scales. It is therefore essential to know how fluid flow in such fracture networks responds to the elevated pressures found at depth. Here, we report results from an investigation of changes in fluid permeability, and associated changes in P-wave and S-wave velocities, at elevated effective pressure for intact, macro-fractured and micro-fractured samples of Seljadur basalt.

In all cases, permeability decreases and both wave velocities increase with increasing effective pressure. Permeability decreases were smallest in the intact material (from approximately 10^{-19}m^2 to 3×10^{-20}m^2), intermediate in the micro-fractured material (from approximately 5×10^{-17}m^2 to 1×10^{-17}m^2) and largest in the macro-fractured material (from approximately 3×10^{-15}m^2 to 9×10^{-19}m^2). For material containing both micro-fractures and macro-fractures, the closure of macro-fractures dominated the permeability reduction at low pressure, with the closure of micro-fractures exerting an increasing influence at higher pressure.

1. Introduction

Fractures are ubiquitous on all scales in crustal rocks. In the upper crust, the presence of fractures influences significantly the physical and transport properties of rock (Walsh, 1981; Gueguen et al., 1997). The existence of fractures makes rock more compliant, and also makes rock more permeable if they are connected together in a percolating network. It is therefore important to investigate how different scales and types of fracture influence the physical and transport properties of rock.

This is important because knowledge of rock physical and transport properties, and their evolution with pressure and stress, is essential to understand both hazardous natural phenomena such as volcanic eruptions and earthquake ruptures, and potentially hazardous geo-engineering projects such as long-term sub-surface storage of hydrocarbons and hazardous waste. That is because the presence of water and other aqueous solutions in rock fractures leads to time-dependent deformation driven by rock-fluid chemical interactions (e.g. see reviews by Anderson and Grew, 1977; Atkinson, 1982, 1984; Atkinson and Meredith, 1987). These studies have demonstrated that the growth rate (velocity) of fractures increases with increasing humidity (Meredith and Atkinson, 1985; Nara and Kaneko, 2005, 2006; Nara et al., 2010a) and in the presence of liquid water (Waza et al., 1980; Sano and Kudo, 1992; Nara et al., 2009, 2010b). Since most crustal rocks contain networks of distributed fractures (Brace et al., 1972; Sprunt and Brace, 1974; Kranz, 1983), and these provide the principal pathways for fluid flow (Koudina et al., 1998; Chaki et al., 2008), it is essential to know how fluids are able to migrate through these networks. However, we also know that fractures can be closed by the application of an elevated pressure and, conversely can be extended by the application of an increased differential stress.

Many efforts have therefore been made to study the change in fluid permeability associated with increasing pressure in crystalline, igneous rocks containing pre-existing networks of micro-fractures, for example in granite (Pratt et al.,1977; Kiyama et al., 1996; Kato et al., 2002; Benson et al., 2006a, b; Nasseri et al., 2009) and basalt (Vinciguerra et al., 2005; Benson et al., 2006b). However, although we know that rocks contain fractures at all scales (i.e., both micro-fractures and

macro-fractures), we know of no previous investigation of the comparative influence of micro-fractures and macro-fractures in controlling permeability in a single rock type. In this study, we have therefore investigated the change in permeability as a function of increasing effective stress in a rock with no visible micro-fractures in its as-received state; Seljadur basalt from south-west Iceland. We have made measurements on samples of intact material, on samples in which we have introduced macro-fractures by mechanical splitting, and on samples in which we have introduced micro-fractures by thermal stressing. As a complementary measure of the crack damage introduced into our samples, we also measured the changes in P-wave and S-wave velocities with increasing effective pressure during our experiments.

2. Experimental material and methodology

2.1 Sample material

All measurements were made on samples of Seljadur basalt (SB), a fresh, columnar-jointed,
intrusive basalt from south-west Iceland. A scanning electron microscope (SEM) image of intact SB
is given in Fig. 1. The rock comprises plagioclase feldspar and pyroxene with some accessory
minerals in a glassy matrix, and has been categorized it as a tholeitic basalt (Eccles et al., 2005).
The SB used in this study has a porosity of 4 % (measured using the ISRM suggested water
saturation method), but no visible pre-existing micro-fractures. This results in a low initial
permeability (approximately 10^{-19} m^2). Samples were cored from a single block of material to a
diameter of 38.1 mm and then ground flat and parallel within $\pm$ 0.02 mm to a nominal length of 40
mm.

We should point out here that all of the samples used in this study were from a different batch of
SB from that for which data are reported in Vinciguerra et al. (2005), but collected from the same
quarry several years later. The earlier material had a porosity of around 1 % and a commensurately
lower initial permeability of 5×10^{-21} m^2.

2.2 Measurement methodology

Permeabilities were measured in a servo-controlled permeameter using the steady-state flow
method. A schematic diagram of the permeameter system used in this study is presented in Fig. 2
(see also, Benson et al., 2005). It comprises a 100 MPa hydrostatic pressure vessel equipped with
dual 70 MPa servo-controlled pore fluid intensifiers. Rubber-jacketed samples are set inside the
pressure vessel between two stainless steel end-caps. The end-caps contain ports to allow pore fluid
to be introduced and distributed to one end of the sample, and to be received and expelled at the
other end. The end-caps also house piezoelectric P-wave and S-wave transducers for the

measurement of axial elastic wave velocities by the ultrasonic transmission method (Birch, 1960).

During permeability measurement, the upstream and downstream intensifiers are set to slightly different control pressures in order to maintain a small, constant pressure difference across the sample. Once steady-state flow is established, permeability can be determined from the rate of fluid flow, the pressure gradient, and the sample dimensions via direct application of Darcy's law. To minimise any temperature-induced pressure fluctuations, the equipment is located within a temperature-controlled laboratory. The temperature was kept constant at 20 ℃ during all experiments.

In this study, we use the simple effective pressure law, $P_{eff} = P_c − a.P_p$, with $a = 1$, where P_c is the applied confining pressure, P_p is the mean pore pressure and P_{eff} is the effective pressure. We varied the effective pressure, P_{eff}, during our experiments by holding the mean pore pressure constant at 4 MPa, and increasing the confining pressure in a series of steps. We estimate that the accuracy of our permeability and wave velocity measurements is 2 % and 1 %, respectively.

2.3 Measurements on sequentially damaged samples

Measurements of permeability and elastic wave velocities were first made, as a function of effective pressure, on an intact sample prepared from the as-received material. Following these initial measurements, we induced macro-fractured samples by splitting the initially intact samples in half axially using a modified Brazil test apparatus at an axial strain rate of $10^{-5}s^{-1}$. These macro-fractured samples were then re-inserted into the permeameter and a second series of permeability measurements made under the same effective pressure conditions. Great care was taken to ensure that the halves of the macro-fractured samples were fully mated with no shear offset. On insertion, the macro-fractures were aligned normal to the polarization direction of the S-wave transducers to better than 5°.

Finally, in order to produce micro-fractured samples we thermally stressed previously intact and macro-fractured samples by heating them slowly to 600℃ or 800℃ inside a tube furnace at

1℃/min to induce thermal cracking. Samples were held at the maximum temperature for 1 hour before cooling to ambient temperature at the same rate. Measurements of permeability and elastic wave velocities were then made on the micro-fractured samples over the same range of effective pressures.

2.4 Imaging macro-fractured samples

Before proceeding to measure the permeabilities and elastic wave velocities of our macro-fractured samples, we used a micro-focus X-ray CT scanner with a spatial resolution of 5 μm to image the induced macro-fractures. The scanner used was the same instrument as that for which results are reported by Kawaragi et al. (2009) and Fukuda et al. (2010). Cross-sectional images were taken across the mid-plane of the samples using the minimum thickness setting of 0.065 mm.

X-ray CT images of two macro-fractured sample of SB are presented in Fig. 3. In these images, darker and lighter shades represent lower and higher densities, respectively. Fractures and pores therefore appear darker than the surrounding matrix. We observe that Brazil test splitting has produced two patterns of macro-fracturing; either a single dominant macro-fracture (Fig. 3a) or a set of three macro-fractures comprising a relatively straight central fracture and two adjacent fractures forming an hour-glass shape (Fig. 3b). We have commonly observed the fracture pattern seen in Fig. 3b in previous Brazil tests on fine-grained, brittle rocks in our laboratory. Use of the minimum thickness setting has also allowed individual pores to be observed. These are relatively sparse and unconnected.

During subsequent permeability measurements, the direction of fluid flow was parallel to the macro-fracture planes. For the elastic wave velocity measurements, P-waves propagated parallel to the macro-fracture planes and S-waves also propagated parallel to the macro-fractures but with their polarization direction normal to the macro-fracture planes.

3. Experimental results

3.1 Macro-fractured samples

Changes in the permeability, P-wave velocity and S-wave velocity of intact and macro-fractured samples of SB as a function of increasing effective pressure are shown in Fig. 4. Fig. 4a shows that the initial permeability of intact SB (sample SB(I)) is very low at approximately 10^{-19} m^{-2}, and that it decreases only marginally as P_{eff} is increased from 5 to 90 MPa. These observations reflect the paucity of pre-existing fractures in the as-received material. By contrast, the permeability of the sample with a single macro-fracture (SB(1F)) (Fig. 3a) is some 3.5 orders of magnitude higher at $P_{eff} = 5$ MPa, while the sample with the three macro-fractures (SB(3F)) (Fig. 3b) is about 4.5 orders of magnitude higher at the same pressure. As might be expected, the permeabilities of the macro-fractured samples decrease much more rapidly with increasing P_{eff} than that for the intact sample, so that at the higher pressures the permeabilities of the two macro-fractured samples are essentially equal and less than 2 orders of magnitude greater than that of the intact sample.

Fig. 4b shows that the P-wave velocity increases only slightly with increasing pressure for all three samples. Not only are the increases very similar for both intact and macro-fractured samples, at around 3 %, but the absolute velocity values are also very similar. These similarities are entirely as expected, since both the propagation direction and the particle motion of the P-waves are parallel to the macro-fracture planes. Hence, the macro-fractures exert little influence on P-wave propagation in this direction.

Similarly, Fig. 4c shows that the S-wave velocity in sample SB(I) also increases by only about 4 % as effective pressure is increased from 5 to 90 MPa. However, in contrast to the P-wave velocities, the S-wave velocities for the both macro-fractured samples are demonstrably lower than that for the intact sample at every pressure. Furthermore, the S-wave velocity for sample SB(3F) is consistently lower than that for sample SB(1F). Again, these observations are entirely as expected, since although the S-wave propagation direction is parallel to the macro-fracture planes, the particle

motion is polarized normal to those planes. Hence, the macro-fractures exert a significantly greater influence on S-wave propagation than for P-wave propagation. Not only that, but we also found that we could not get sufficient signal amplitude to measure the S-wave velocity at the lower effective pressures because of signal attenuation caused by the presence of the macro-fracture(s). For sample SB(1F), we could not get a good signal below 20 MPa, and for sample SB(3F), we could not get a good signal below 40 MPa (Fig. 4c).

These results are therefore all consistent with the idea that the macro-fractures close progressively with increasing effective stress. The macro-fracture apertures exert a large influence on fluid permeability and a significant influence on S-wave velocities for waves polarized normal to their length.

3.2 Micro-fractured samples

Since X-ray CT scanning does not have sufficient resolution to allow us to observe the micro-fractures induced in our samples of SB subjected to thermal stressing, we measured the P-wave velocities of unsaturated intact and thermally-stressed samples at ambient pressure, as an indicator of increased micro-fracture damage, before commencing measurements at pressure in the permeameter. The intact sample had an axial P-wave velocity of 5.65 km.s^{-1}. After heating to 600℃, the velocity decreased markedly to 4.69 km.s^{-1} and, after heating to 800℃, the velocity decreased further to 4.33 km.s^{-1}. This suggests that significantly more thermal micro-fracture damage was induced in the sample heated to 800℃ than in the sample heated to 600℃.

Changes in the permeability, P-wave velocity and S-wave velocity of intact and micro-fractured samples of SB as a function of increasing effective pressure are shown in Fig. 5 (the data for the intact sample is the same as presented in Fig. 4). Fig. 5a shows that, once again, the introduction of cracks leads to increases in fluid permeability; albeit micro-fractures rather than macro-fractures in this case. The initial permeability of the sample heated to 600℃ (SB(600)) is some 20 times higher than that for sample SB(I), and that for the sample heated to 800℃ (SB(800)) is close to 500 times

higher. As for the macro-fractured samples, the permeabilities of the micro-fractured samples decreased with increasing effective pressure, indicating crack closure.

Fig. 5b shows that the pattern of behaviour of P-wave velocities in the micro-fractured rock samples is significantly different from that seen for the macro-fractured samples (Fig. 4b). The P-wave velocity in sample SB(600) is about 6 % lower than that for sample SB(I) at $P_{\text{eff}} = 5$ MPa, while that for sample SB(800) is close to 12 % lower at the same pressure. These velocity differences decrease in an essentially identical manner with increasing effective pressure so that by 90 MPa the P-wave velocity in SB(600) is only about 1 % lower than in SB (I) and in SB(800) it is about 6 % lower. This supports the suggestion that thermal stressing to 800°C induces far more micro-fracturing than thermal stressing to 800°C. However, while the micro-fractures exert a smaller influence on permeability than the macro-fractures, it is clear from the changes in both permeability and P-wave velocity with increasing effective pressure that the micro-fractures are considerably more difficult to close. Fig. 5c shows that the pattern of behaviour of S-wave velocities in the micro-fractured samples is essentially the same as that seen for P-wave velocities in Fig. 5b.

The similarities between the changes observed in P-wave and S-wave velocities occur even though the particle motions are orthogonal. This suggests that, in contrast to the highly oriented macro-fractures (Fig. 3), the micro-fractures induced by thermal stressing in our samples are essentially isotropically distributed. This suggestion is entirely consistent with the results of Vinciguerra et al. (2005), who reported an isotropic distribution of thermal microcracks and isotropic elastic wave velocities in their thermally stressed samples of Seljadur basalt.

4. Discussion

We have seen from the results presented in Figs. 4 and 5 how the introduction of macro-fractures and micro-fractures into a rock with an essentially unfractured matrix can change the fluid permeability quite dramatically. It is clear that a few, long, low-aspect-ratio macro-fractures increase permeability much more than a much greater number of shorter, high aspect-ratio micro-fractures. However, the dominant influence of the macro-fractures is greatest at low effective pressure and when fluid flow is parallel to their long axes. Due to their low aspect ratio, macro-fractures are relatively easily closed by an increase in effective pressure, so that their overall influence declines at higher pressures. In contrast, while a distributed network of micro-fractures exerts a smaller influence on permeability overall, that influence appears to be maintained even at the highest effective pressures because their high aspect ratio makes them more difficult to close. However, we know that many natural materials, including rocks, contain fractures at different scales (i.e., both micro-fractures and macro-fractures).

Ideally, therefore we would like to understand the interplay between these two fracture populations and how that may influence the change in permeability with increasing effective pressure (c.f. increasing depth in the crust). We therefore prepared a further sample of SB containing both macro-fractures and micro-fractures by thermally stressing sample SB(3F) by slow heating to 800℃. We then measured the fluid permeability and elastic wave velocities for this sample as a function of effective pressure in exactly the same way as described above for our other samples.

The results of these measurements are presented in Fig. 6. The data for the intact sample, the macro-fractured sample and the micro-fractured sample in Fig. 6 are the same as those for sample SB(I) and sample SB(3F) in Fig. 4 and SB(800) in Fig. 5. We note in Fig. 6a that the permeability for the macro- and micro-fractured sample (SB(MM)) is essentially the same as that for sample SB(3F) at the lowest effective pressure (5 MPa). This observation confirms our earlier suggestion that low-aspect-ratio macro-fractures dominate fluid flow under these conditions. The addition of a

population of high-aspect-ratio micro-fractures appears to contribute nothing to the fluid flow.

However, this situation changes dramatically by the time we reach the highest effective pressure (90

MPa). Here, the macro-fractures and micro-fractures appear to contribute essentially equally to the

increase in permeability with respect to the intact sample. This is because the rate of permeability

decrease with increasing effective pressure is much lower for sample SB(MM) than for sample

SB(3F). We suggest that this occurs simply because the high-aspect-ratio micro-fractures are more

difficult to close than the low-aspect-ratio macro-fractures. We further observe that the permeability

for sample SB(800) is much lower than for sample SB(MM) at low pressure, but that the

permeabilities are virtually the same at the highest effective pressure, confirming the above

suggestion that the open micro-fractures increasingly dominate the permeability as effective

pressure in increased. However, it is also clear from Fig. 6a that both the macro-fractures and the

micro-fractures are still open at 90 MPa. We therefore suggest that if such measurements were

continued to even higher effective pressures then the micro-fractures would become even more

dominant over the macro-fractures in controlling fluid permeability. In the same way as for Figs. 4

and 5, the wave velocity data of Figs. 6b and 6c support this interpretation of permeability

evolution.

However, while these are robust observations, it is also important to quantify how different

fractures populations influence fluid permeability in rocks. First we consider the influence of

micro-fractures using the model of Gueguen and Dienes (1989), who proposed the following

relationship:

$$k = \frac{2}{15} f w^2 \varsigma \varphi \qquad (1)$$

where, k is the permeability, f is the percolation factor, w is the mean micro-fracture aperture, ς is

their mean aspect ratio, and φ is their volume density. For $0.14 < \varphi < 0.4$, the percolation factor f

can be approximated be the following relation follows (Benson et al., 2006b):

$$f \approx \frac{9}{4} \left(\frac{\pi^2}{4} \varphi - \frac{1}{3} \right)^2 \qquad (2)$$

Hence the permeability of a micro-fractured solid can be related to the aperture, aspect ratio and density of the micro-fractures.

There are several methods of determining the micro-fracture density of a solid. Here we compare two different methods; Hudson's model (Hudson, 1980, 1981) and the New Self Consistent Scheme (NSCS) (Yamamoto, 1981; Nara and Kaneko, 2006). Since Hudson's model is a "dilute solution", we can use it only for the case where the micro-fracture density is low and fractures are non-interacting. By contrast, the NSCS can be used for higher micro-fracture densities because it takes account of micro-fracture interactions. In order to determine the NSCS micro-fracture density we need an estimate of the aspect ratio of the micro-fractures. For simplicity, we make use of previously measured parameters for micro-fractured basalt. Vinciguerra et al. (2005) showed that the P-wave velocity in experimentally thermally fractured Seljadur basalt was very similar to that in naturally thermally fractured Etnean basalt, and Benson et al. (2006b) showed that the aspect ratio of micro-fractures in Etnean basalt remained essentially constant at approximately 0.001 when the permeability was lower than 10^{-16} m^2 and the crack density was lower than 0.4. Since both of these conditions are met in our case, we assume a micro-fracture aspect ratio of 0.001 in our calculations.

As reported above, the P-wave velocities in samples SB(800), SB(600) and SB(I), in dry conditions and ambient pressure, are 4.33, 4.69 and 5.65 km/s, respectively. Using these values and assuming that the Young's modulus and Poisson's ratio of the unfractured basalt matrix are 100 GPa and 0.22, respectively (following Benson et al., 2006b), the crack densities of samples SB(800), SB(600) and SB(I) were determined using both Hudson's model and the NSCS method. The calculated values are summarized in Table 1. Following this, the relations between permeability k and micro-fracture density φ were calculated for different values of crack aperture w from Eqs. (1) and (2), within the range of $0.14 < \varphi < 0.4$.

The results are shown in Fig. 7, together with the permeabilities for SB(800) and SB(600) measured at the lowest effective pressure (5 MPa). Using the value for φ determined from the NSCS model, we see in Fig. 7 that the predicted micro-fracture apertures for samples SB(600) and SB(800) are in the range of 0.4 ~ 1.1 μm, which is very similar to the range of 0.5 ~ 0.8 μm

reported for basalt by Benson et al. (2006b) from SEM observations. By contrast, the Hudson

model predicts considerably larger apertures in the range 1.5 ~ 4.0 μm. We therefore suggest that

the NSCS method provides better estimates of fracture density and aperture because it takes account

of interactions between micro-fractures. It is also apparent from Fig. 7 that the higher permeability

of sample SB(800) over sample SB(600) is due to it having a higher micro-fracture density.

However, for the NSCS data, the fracture density increases by only 30 % from 0.30 to 0.39 while

the fracture aperture increases by 175 % from 0.4 to 1.1 μm. This suggests that the higher fracture

density (and associated higher permeability) is primarily due to an increase in fracture aperture.

Second, we consider the influence of macro-fractures on permeability using the model of Walsh

(1981) who proposed the following expression to describe the effect of pressure on fluid flow

through macro-fractures:

$$k^{1/3} = A - B \ln P_{\text{eff}} \qquad (3)$$

where A and B are empirical constants. The relations between $k^{1/3}$ and P_{eff} for macro-fractured

samples SB(3F) and macro- plus micro-fractured sample SB(MM)) are presented in Fig. 8. As noted

earlier, we see that the permeability for sample SB(MM) is essentially the same as that for sample

SB(3F) at the lowest effective pressure, suggesting the dominance of macro-fractures over

micro-fractures. However, the relative slopes of the $k^{1/3}$ vs. P_{eff} curves show that the permeability

for SB(3F) decreases much more rapidly with increasing effective pressure. We also note that there

is a significant change in the slope for SB(3F) at an effective pressure of around 20 MPa, and

interpret this as due to closure of the low-aspect-ratio macro-fractures in this sample. For sample

SB(MM), containing both micro- and macro-fractures, we also observe a significant change in slope

at a slightly higher effective pressure of around 30 MPa. Since we have seen that the

low-aspect-ratio macro-fractures are essentially closed at this pressure, we suggest that the

high-aspect-ratio micro-fractures increasingly dominate the fluid permeability at higher pressure.

Due to this closure of the macro-fractures, we suggest that the Walsh model breaks down at

effective pressures greater than 20 ~ 30 MPa as micro-fractures start to dominate the fluid flow

behaviour.

Overall, the results reported here clarify how different fracture populations within the same rock influence the permeability and elastic wave velocities in that rock. While permeability always decreases as a function of increasing effective pressure in fractured rock (whether macro-fractures, micro-fractures or a combination of the two), the rate of change of permeability is also generally seen to decrease with increasing effective pressure. However, that rate of change can alter significantly when there is a change in the dominance of one fracture population over another. We therefore suggest that any attempt at predicting permeability evolution in rock must first quantify and characterize the size and orientation of fracture populations in the rock and their sensitivity to changes in effective pressure.

5. Conclusions

For all samples studied, we found that permeability always decreased with increasing effective pressure. The decreases were smallest for intact samples, intermediate for the micro-fractured samples, and largest for the macro-fractured samples. For the sample with both macro-fractures and micro-fractures, we found that closure of the macro-fractures dominated the permeability reduction at the lower effective pressures, but that closure of the micro-fractures exerted an increasing relative influence on permeability reduction with increasing effective pressure. We therefore conclude that macro-fractures with low aspect ratios close more easily with increasing pressure, so that micro-fractures with high aspect ratios increasingly dominate the permeability at higher pressures because they are more difficult to close. The associated variations measured in P-wave and S-wave velocities support this interpretation.

Acknowledgements

References

Anderson, O.L., Grew, P.C., 1977. Stress corrosion theory of crack propagation with applications to geophysics. Rev. Geophys. Space Phys. 15, 77-104.

Atkinson, B.K., 1982. Subcritical crack propagation in rocks: theory, experimental results and applications. J. Struct. Geol. 4, 41-56.

Atkinson, B.K., 1984. Subcritical crack growth in geological materials. J. Geophys. Res. 89, 4077-4114.

Atkinson, B.K., Meredith, P.G., 1987. The theory of subcritical crack growth with applications to minerals and rocks. In: Fracture Mechanics of Rock. London: Academic Press; 1987. pp.111-166.

Benson, P.M., Meredith, P.G., Platzman, E.S., White, R.E., 2005. Pore fabric shape anisotropy in porous sandstones and its relation to elastic wave velocity and permeability anisotropy under hydrostatic pressure. Int. J. Rock Mech. Min. Sci. 42, 890-899.

Benson, P.M., Meredith, P.G., Schubnel, A., 2006a. Role of void space geometry in permeability evolution in crustal rocks at elevated pressure. J. Geophys. Res. 111, B12203, doi: 10.1029/2006JB004309.

Benson, P., Schubnel, A., Vinciguerra, S., Trovato, C., Meredith, P., Young, R. P., 2006b. Modeling the permeability evolution of microcracked rocks from elastic wave velocity inversion at elevated isotropic pressure. J. Geophys. Res. 111, B04202, doi: 10.1029/2005JB003710.

Birch, F., 1960. The velocity of compressional waves in rocks to 10 kirobars, Part 1. J. Geophys. Res. 65, 1083-1102.

Brace, W.F., Silver, E., Hadley, K., Goetze, C., 1972. Cracks and Pores: a closer look. Science 178, 162-164.

Chaki, S., Takarli, M., Agbodjan, W.P., 2008. Influence of thermal damage on physical properties of a granite rock: porosity, permeability and ultrasonic wave evolutions. Constr. Build. Mater. 22, 1456-1461.

Eccles, D., Sammonds, P.R., Clint, O.C., 2005. Laboratory studies of electrical potential during

rock failure. Int. J. Rock Mech. Min. Sci. 42, 933-949.

Fukuda, D., Nara, Y., Mori, D., Kaneko, K., 2010. Sealing behavior of fracture in cementitious

material with micro-focus X-ray CT. Proc. GeoX 2010, pp.148-155, New Orleans, Louisiana,

USA, March 1-3, 2010.

Gueguen, Y. and Dienes, J., 1989. Transport properties of rocks from statistics and percolation.

Math. Geol. 21, 1-13.

Gueguen, Y., Chelidze, T., Le Ravalec, M., 1997. Microstructures, percolation thresholds, and rock

physical properties. Tectonophys. 279, 23-35.

Hudson, J.A., 1980. Overall properties of a cracked solid. Math. Proc. Camb. Phil. Soc. 88,

371-384.

Hudson, J.A., 1981. Wave speeds and attenuation of elastic waves in material containing cracks.

Geophys. J. R. Astr. Soc. 64, 133-150.

Kato, M., Sanoki, S., Miyagi, A., Takahashi, M., Kaneko, K., 2002. Anisotropic permeability of

granite. Proc. 3rd Korea-Japan Joint Symposium on Rock Engineering, pp.851-858, Seoul,

Korea, July 22-24, 2002.

Kawaragi, C., Yoneda, T., Sato, T., Kaneko, K., 2009. Microstructure of saturated bentonites

characterized by X-ray CT observations. Eng. Geol. 106, 51-57.

Kiyama, T., Kita, H., Ishijima, Y., Yanagidani, T., Aoki, K., Sato, T., 1996. Permeability in

anisotropic granite under hydrostatic compression and triaxial compression including

post-failure region. Proc. 2nd North American Rock Mechanics Symposium, pp.1643-1650,

Montreal, Quebec, Canada, June 19-21, 1996.

Koudina, N., Gonzalez Garcia, R., Thovert, J. –F., Adler, P.M., 1998. Permeability of

three-dimensional fracture networks. Phys. Rev. E 57, 4466-4479.

Kranz, R.L., 1983. Microcracks in rocks: a review. Tectonophys. 100, 449-480.

Meredith, P.G., Atkinson, B.K., 1985. Fracture toughness and subcritical crack growth during

high-temperature tensile deformation of Westerly granite and Black gabbro. Phys. Earth Planet.

Inter. 39, 33-51.

Nara, Y., Kaneko, K., 2005. Study of subcritical crack growth in andesite using the Double Torsion test. Int. J. Rock Mech. Min. Sci. 42, 521-530.

Nara, Y., Kaneko, K., 2006. Sub-critical crack growth in anisotropic rock. Int. J. Rock Mech. Min. Sci. 43, 437-453.

Nara, Y., Takada, M., Igarashi, T., Hiroyoshi, N., Kaneko, K., 2009. Subcritical crack growth in rocks in an aqueous environment. Explor. Geophys. 40, 163-171.

Nara, Y., Hiroyoshi, N., Yoneda, T., Kaneko, K. 2010a. Effects of relative humidity and temperature on subcritical crack growth in igneous rock. Int. J. Rock Mech. Min. Sci. 47, 640-646.

Nara, Y., Takada, M., Mori, D., Owada, H., Yoneda, T., Kaneko, K., 2010b. Subcritical crack growth and long-term strength in rock and cementitious material. Int. J. Fract. 164, 57-71, DOI: 10.1007/s10704-010-9455-z.

Nasseri, M.B.H., Schubnel, A., Benson, P.M., Young, R.P., 2009. Common evolution of mechanical and transport properties in thermally cracked Westerly granite at elevated hydrostatic pressure. Pure Appl. Geophys. 166, 927-948.

Pratt, H.R., Swolfs, H.S., Brace, W.F., Black, A.D., Handin, J.W., 1977. Elastic and transport properties of an in situ jointed granite. Int. J. Rock Mech. Min. Sci. & Geomech. Abstr. 14, 35-45.

Sano, O., Kudo, Y., 1992. Relation of fracture resistance to fabric for granitic rocks. Pure Appl. Geophys. 138, 657-677.

Sprunt, E.S., Brace, W.F., 1974. Direct observation of microcavities in crystalline rocks. Int. J. Rock Mech. Min. Sci. & Geomech. Abstr. 11, 139-150.

Vinciguerra, S., Trovato, C., Meredith, P.G., Benson, P.M., 2005. Relating seismic velocities, thermal cracking and permeability in Mt. Etna and Iceland basalts. Int. J. Rock Mech. Min. Sci. 42, 900-910.

Walsh, J.B., 1981. Effect of pore pressure and confining pressure on fracture permeability. Int. J.

Rock Mech. Min. Sci. & Geomech. Abstr. 18, 429-435.

Waza, T., Kurita, T., Mizutani, H., 1980. The effect of water on the subcritical crack growth in

silicate rocks. Tectonophys. 67, 25-34.

Yamamoto, K., 1981. Theoretical determination of effective elastic constants of composite and its

application to seismology. PhD Thesis, Tohoku University.

Figure captions

Fig. 1. Scanning Electron Microscope photomicrograph of intact Seljadur basalt.

Fig. 2. Schematic diagram of the permeameter and elastic wave velocity measurement system used

for all measurements in this study.

Fig. 3. Micro-focus X-ray CT images of macro-fractured Seljadur basalt samples.

(a): sample SB(1F) with a single axial macro-fracture, (b): sample SB(3F) containing three

axial macro-fractures

Fig. 4. Measurements of: (a) permeability, (b) P-wave velocity and (c) S-wave velocity with

increasing effective pressure for intact and macro-fractured samples of Seljadur basalt; SB(I),

SB(1F) and SB(3F), respectively.

Fig. 5. Measurements of: (a) permeability, (b) P-wave velocity and (c) S-wave velocity with

increasing effective pressure for intact and micro-fractured samples of Seljadur basalt; SB(I),

SB(600) and SB(800), respectively.

Fig. 6. Measurements of: (a) permeability, (b) P-wave velocity and (c) S-wave velocity with

increasing effective pressure for intact, macro-fractured, micro-fractured and macro-fractured plus

micro-fractured samples of Seljadur basalt; SB(I), SB(3F), SB(800) and SB(MM), respectively.

Fig. 7. Relation between permeability and micro-fracture density calculated from the

Gueguen-Dienes model for different crack apertures (w). Open symbols use micro-fracture densities

from Hudson's model, and solid symbols use micro-fracture densities from the NSCS model.

Triangles are measured permeabilities for sample SB(600), and circles are measured permeabilities

for sample SB(800).

Fig. 8. Plots of the relation between the cube route of permeability and effective pressure from

Walsh's model. Open symbols are measured data for the samples indicated.

Table

Table 1. Density of micro-fracture in intact and micro-fractured basalt

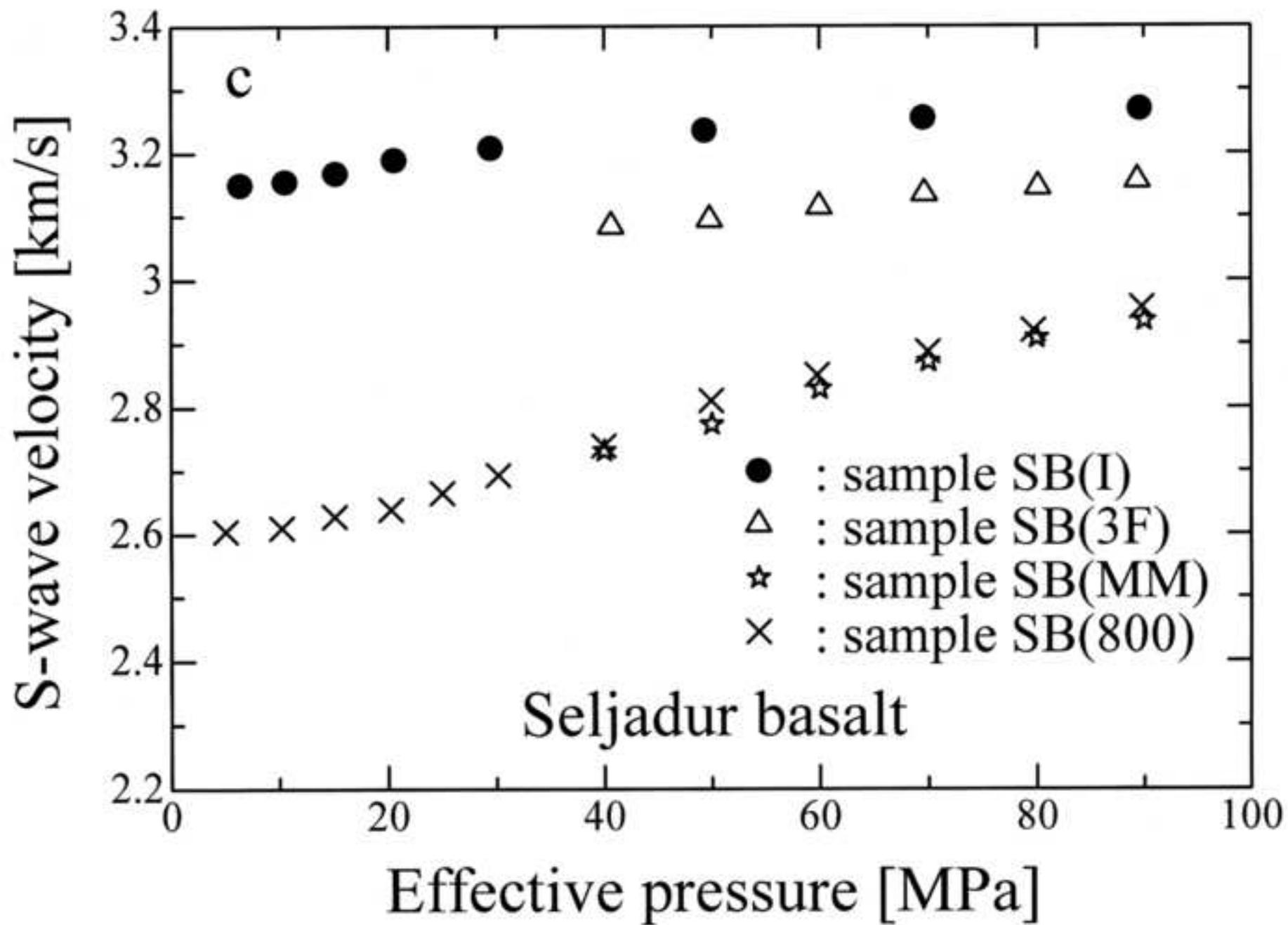|	φ (Hudson's model)	φ (NSCS)
SB(I)	0.082	0.10
SB(600)	0.19	0.30
SB(800)	0.23	0.39

Figure2

Figure4b
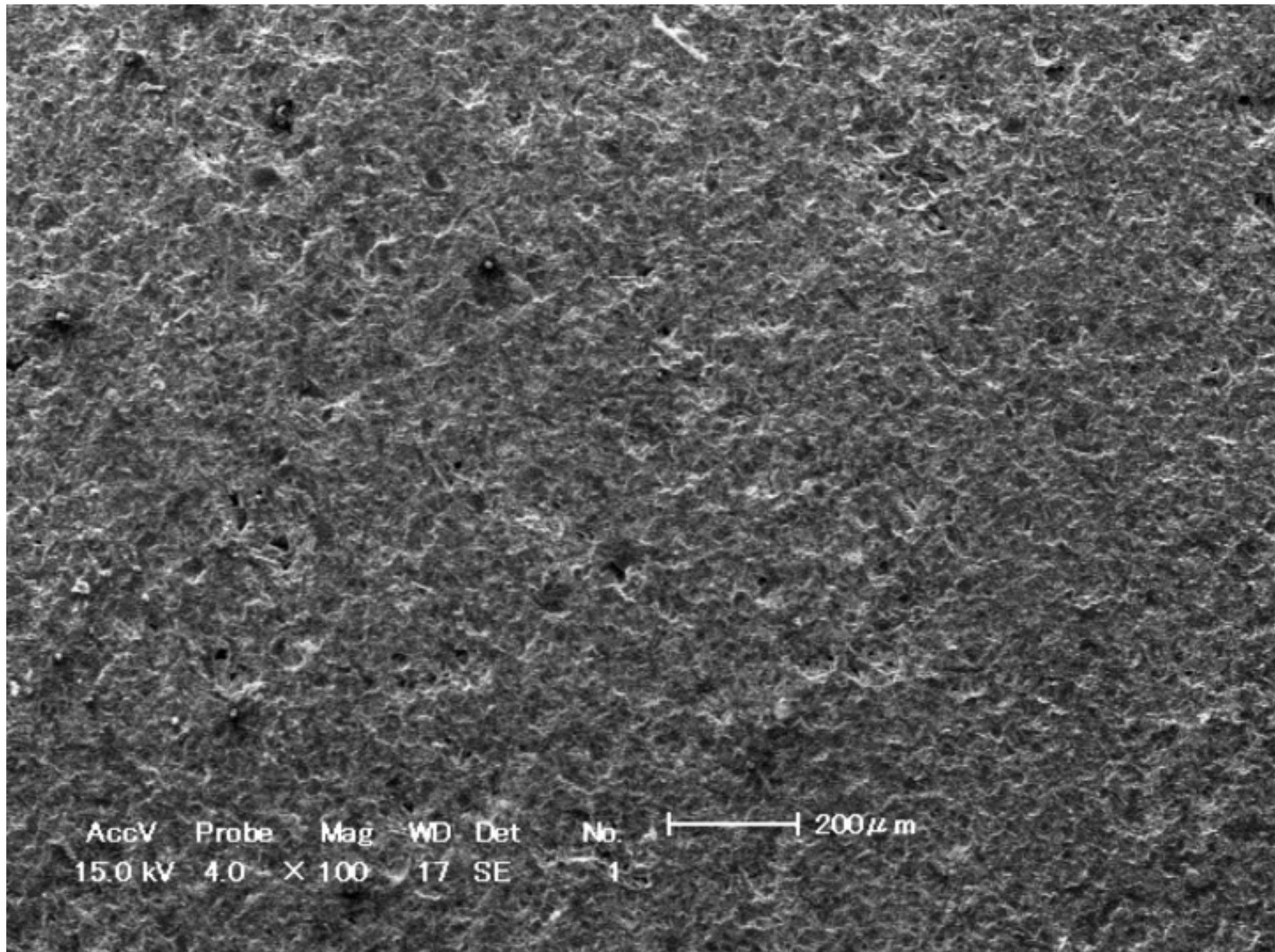
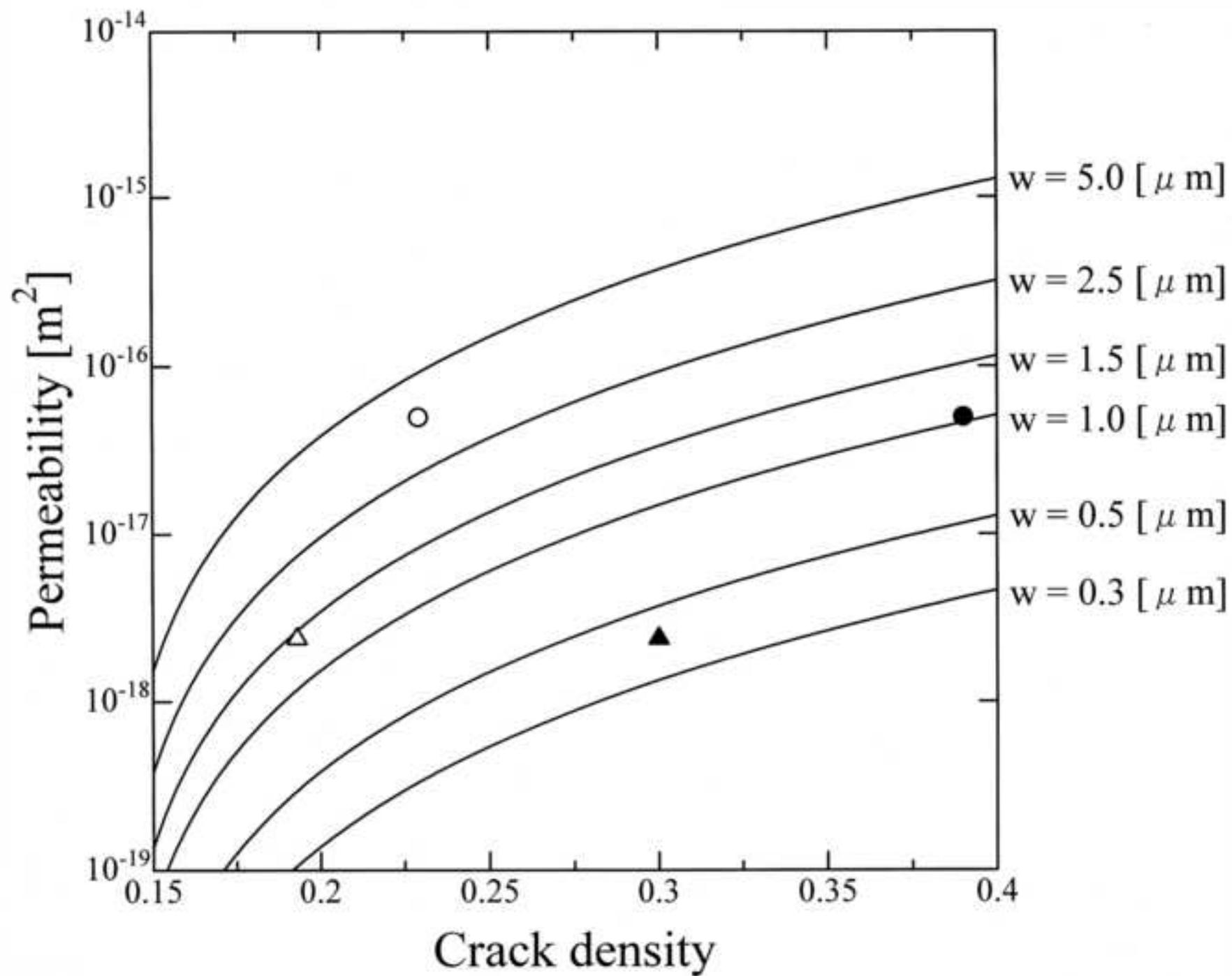Figure 5b

Figure5c

Figure7
Click here to download high resolution image

Figure8
Click here to download high resolution image